

An X-ray and Radio Study of the Varying Expansion Velocities in Tycho's Supernova Remnant

Brian J. Williams,¹ Laura Chomiuk,² John W. Hewitt,³ John M. Blondin,⁴ Kazimierz J.
Borkowski,⁴ Parviz Ghavamian,⁵ Robert Petre,⁶ Stephen P. Reynolds,⁴

Received _____; accepted _____

¹CRESST/USRA and X-ray Astrophysics Laboratory, NASA GSFC, 8800 Greenbelt Road, Greenbelt, MD, Code 662, brian.j.williams@nasa.gov

²Department of Physics and Astronomy, Michigan State University, East Lansing, Michigan 48824, USA

³University of North Florida, Department of Physics, 1 UNF Drive, Jacksonville, FL 32224, USA

⁴Department of Physics, North Carolina State University, Raleigh, NC 27695

⁵Department of Physics, Astronomy, and Geosciences, Towson University, Towson, MD 21252

⁶NASA GSFC, X-ray Astrophysics Laboratory, Greenbelt, MD 20771, USA

ABSTRACT

We present newly obtained X-ray and radio observations of Tycho’s supernova remnant using *Chandra* and the Karl G. Jansky Very Large Array in 2015 and 2013/14, respectively. When combined with earlier epoch observations by these instruments, we now have time baselines for expansion measurements of the remnant of 12-15 year in the X-rays and 30 year in the radio. The remnant’s large angular size allows for proper motion measurements at many locations around the periphery of the blast wave. We find, consistent with earlier measurements, a clear gradient in the expansion velocity of the remnant, despite its round shape. The proper motions on the western and southwestern sides of the remnant are about a factor of two higher than those in the east and northeast. We showed in an earlier work that this is related to an offset of the explosion site from the geometric center of the remnant due to a density gradient in the ISM, and using our refined measurements reported here, we find that this offset is $\sim 23''$ towards the northeast. An explosion center offset in such a circular remnant has implications for searches for progenitor companions in other remnants.

1. Introduction

Tycho’s supernova remnant (SNR; hereafter Tycho), is the remnant of the SN observed in 1572 (Stephenson & Green 2002), first characterized by Baade (1945) as a “Type I” SN. Rest et al. (2008) identified light echoes from the event, and spectroscopy of these echoes by Krause et al. (2008) matched the spectrum to a normal SN Ia. Many authors have adopted a distance of 2.3 kpc, suggested by Chevalier et al. (1980) based on an analysis of optical observations of nonradiative shocks, and by Albinson et al. (1986), based on H I absorption. Distances of over 4 kpc have also been reported, based on higher-resolution H I data (Schwarz et al. 1995). In an earlier work

(Williams et al. 2013, hereafter W13), we favored a distance of 3.5 kpc, based on comparisons of hydrodynamic simulations with data. There, we examined the infrared (IR) colors of the remnant, fitting models of warm dust to the *Spitzer* broad-band fluxes. These models are sensitive to the post-shock gas density, and we found a variation in density as a function of azimuthal angle around the shell, with densities in the east and northeast several times higher than in the west and southwest.

SNe Ia are believed to result from a thermonuclear explosion of a white dwarf destabilized by mass transfer in a binary system, but the nature of the binary is unknown. The two leading models are the single-degenerate (SD) and double-degenerate (DD) scenarios. In the SD channel (Whelan & Iben 1973), a white dwarf accretes matter from a non-degenerate companion and explodes when it reaches the Chandrasekhar limit. In this scenario, the companion star should survive, though evidence for this via searches for this companion star in Type Ia SNRs is scant (Schaefer & Pagnotta 2012). The DD channel (Webbink 1984), on the other hand, involves an explosion triggered by the merger of two white dwarfs, and no surviving companion is expected.

While Tycho is clearly round in shape, a departure from spherical symmetry is suggested by measurements of the proper motion of the shell. Reynoso et al. (1997) used radio images from 1983/84 and 1994/95 and found that the shock velocity varies by a factor of three as a function of position around the shell. Hughes (2000) confirmed these azimuthal variations from *ROSAT* images. Katsuda et al. (2010) examined *Chandra* images from 2000, 2003, and 2007 to measure the expansion of the remnant at 39 positions around the periphery and determined that the X-ray proper motions of the forward shock vary by about a factor of two.

The radio and X-ray emission from the forward shock in Tycho both arise from the same physical process, nonthermal synchrotron emission. Electrons are accelerated by turbulent magnetic fields, amplified at the shock front. This acceleration produces a nonthermal “tail” to the particle energy distribution, where electrons reach relativistic energies up to tens of TeV. These

highest energy electrons, spiraling in the magnetic field, produce X-ray synchrotron emission (Reynolds & Keohane 1999), while the radio emission results from particles with energies in the GeV range. While most young remnants exhibit thermal X-ray emission at their forward shock, Hwang et al. (2002) show that in Tycho, the emission at the immediate edge is nonthermal.

In this work, we report on proper motion measurements of the forward shock, made from newly-obtained X-ray and radio data from *Chandra* and the *Karl G. Jansky Very Large Array (VLA)* in 2015 and 2013/14, respectively. While the measurements made by Reynoso et al. (1997) and Katsuda et al. (2010) follow the same general trend, there are discrepancies between them. This is not unexpected, as these were independent groups of authors using different techniques with relatively short time baselines. With much longer time baselines (twice as long in the X-ray band and three times longer in the radio), as well as a consistent approach to the measurements in both, we can greatly reduce the uncertainties and disparities in the previous measurements. Accurate determinations of shock velocities in Tycho are important for the physics of particle acceleration, as electron maximum energies and efficiencies of acceleration and magnetic-field amplification depend on high powers of the velocity.

The X-ray and radio profiles have different shapes, owing to the physics of synchrotron emission. X-ray synchrotron emission is confined to a thin rim that rises sharply at the shock front, only to fall again fairly quickly behind it as a result of synchrotron losses on the electrons, damping of the magnetic field, or both. This phenomenon is discussed at length in Ressler et al. (2014) and Tran et al. (2015) (for Tycho in particular). Radio synchrotron emission results from lower energy electrons with a longer life, and persists well behind the shock front, creating a plateau emission profile.

2. Observations

2.1. X-ray

Chandra has observed Tycho four times prior to our 2015 observations: 50 ks in 2000, 150 ks in 2003 and 2007, and 750 ks in 2009. The 2000 observation used the ACIS-S3 chip, and the positioning of Tycho on the chip resulted in about 25% of it along the southern shell being cut off by the chip edge (Hwang et al. 2002). Subsequent observations used the I-array and cover the entire remnant. For this work, we use the longest time baselines. For most of the remnant, our measurements are made between the 2000 and 2015 data. For the portions in the south that were not covered by the 2000 observation (approximately one third of our regions), we substitute the 2003 epoch.

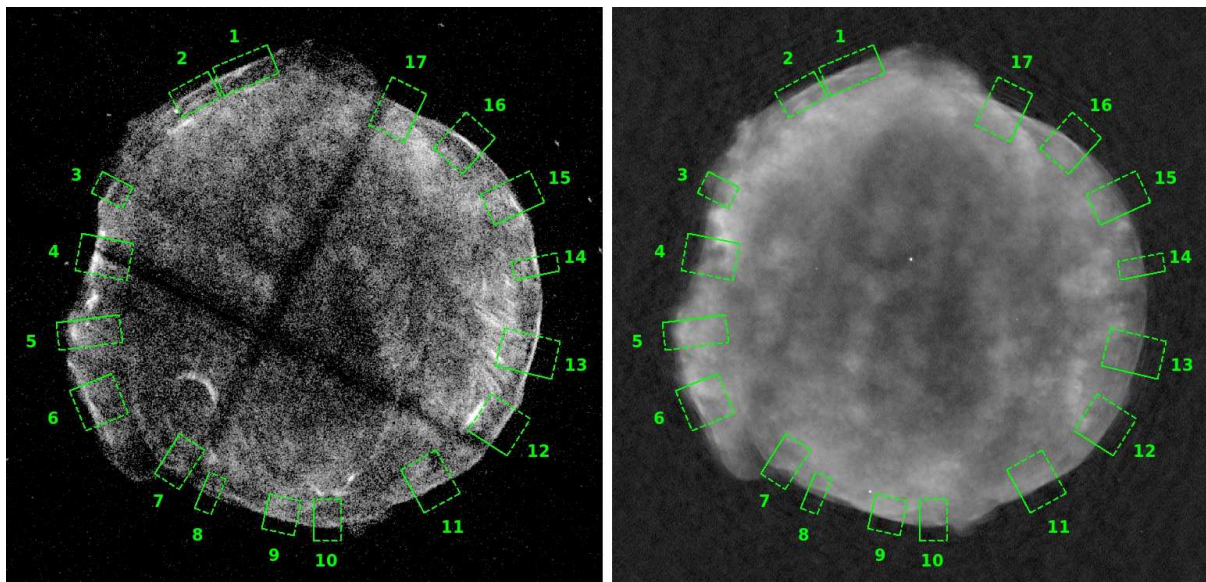


Fig. 1.— Left: *Chandra* 3-8 keV X-ray image of Tycho from 2015, smoothed with a 2-pixel Gaussian. Right: VLA image from 2013. Overlaid on both are the 17 regions in which the proper motion of the shock is measured. Images are $10.8'$ on a side.

We observed Tycho for 150 ks on 2015 Apr 22-24 using the ACIS I-array. The time intervals

from the 2000 and 2003 observations to the 2015 are 14.6 and 12.0 year, respectively. We follow a similar data reduction procedure to Katsuda et al. (2010), using version 4.7 of CIAO and version 4.6.5 of CALDB to process all epochs. We examined the light curves and found no significant background flares. To align all epochs to a common reference frame, we first used the CIAO task `wavdetect` to detect point sources in the field. The tasks `wcs_match` and `wcs_update` then reprojected each events file to identical `wcs` coordinates. We use the deep 2009 observation as the relative “reference” frame to which all other epochs are aligned. We smooth the X-ray images slightly, using a 2-pixel Gaussian. This has virtually no effect on the profile shapes, but significantly decreases the pixel-to-pixel Poisson noise level.

2.2. Radio

We imaged two epochs of L-band (~ 1.4 GHz) observations, both obtained with the VLA in its A, B, C, and D configurations. The first epoch (PI W. van Breugel), from 1983–1984, is published in Reynoso et al. (1997), but is re-imaged here. The second was obtained by our team as part of project VLA/13A-426 (PI J.W. Hewitt), on 2013 Feb 9 (D configuration), 2013 Jun 8 (C configuration), 2013 Sep 28 (B configuration) and 2014 Feb 20 (A configuration). For simplicity, we will refer to these as the “2013” observations (and the first epoch as “1983”). Two other VLA epochs (1994 and 2002) have also been obtained, but we desire the longest time baseline, and only use the 1983 and 2013 data.

Data are edited and calibrated using standard routines in AIPS, and data from all configurations were concatenated in the uv plane using `VBGLU` for the 1983 epoch and `DBCON` for the 2013 epoch. In both epochs, the source J0217+7349 was used for complex gain calibration, while 3C48 was used for absolute flux calibration and, in the case of the 2013 epoch, bandpass calibration. We imaged in AIPS using multi-scale clean in `IMAGR`.

Data in the A configuration were obtained over 1983 Nov 13–14, providing 5.4 hours on source with bandwidth of 3.1 MHz at each of two intermediate frequencies (IFs); IFs were tuned to 1375 and 1385 MHz. B configuration data were observed 1984 Jan 5–7, yielding 4.6 hours on source with bandwidth of 6.2 MHz \times 2 IFs, and IFs are positioned at 1365 and 1442 MHz. C configuration data were obtained on 1983 April 17–18, with one IF at 1375 MHz and 25 MHz of bandwidth; 5.1 hours of on-source time were obtained. D configuration data were obtained on 1983 Jun 18, with 1.8 hours on source and 25 MHz of bandwidth tuned to 1375 MHz. The narrow bandwidths in A and B configurations minimize the effects of bandwidth smearing. We imaged this epoch using a Briggs Robust value of -3 (nearly uniform weighting), yielding a FWHM of the synthesized beam, $1.39'' \times 1.31''$, at a PA = 28.2° .

In each of our 2013 configurations, observations yielded 0.5 hour on source and made use of the full 1 GHz bandwidth of the L band. However, to effectively compare with the 1983 epoch, we only made use of the sixth and seventh spectral windows, which are 64 MHz wide and centered at 1346 and 1410 MHz. We imaged these data with a Briggs Robust value of -5 (uniform weighting) to produce an image with resolution $1.86'' \times 0.88''$ at a PA = 274.7° . Because the observations from the two epochs had different point spread functions, and because both of these were elliptical, we degrade both images to a circular beam of $1.91'' \times 1.91''$ using the AIPS task CONVL. Both the X-ray and radio images are shown in Figure 1.

3. Results

In choosing our measurement regions, we attempt to best match our previous regions in W13, with some modifications necessitated by the data, such as choosing locations where the shock front is “sharpest” (little diffuse emission). We use X-ray data only in the 3–8 keV range for two reasons. First, this eliminates virtually all thermal emission, selecting only the nonthermal synchrotron radiation that defines the shock front. Secondly, this allows for a more

direct comparison with the radio data, where the emission is also synchrotron. Our regions are “projection” boxes in ds9⁷, and range in width from 20-60”, chosen to lie along the shock front. We made our boxes large enough to provide good statistics within the region of interest, but small enough so that the curved shock front remains mostly straight. There are two gaps in our coverage: one at a PA (E of N) of $\sim 45^\circ$ (between boxes 2 and 3) and the other at $\sim 350^\circ$ (between boxes 17 and 1). In these locations, the shock front is too diffuse to get a good profile and a robust proper motion measurement.

Our procedure for measuring the proper motion mirrors that found in Katsuda et al. (2008a), where a fuller description can be found. Other SNR works, such as Winkler et al. (2014) and Yamaguchi et al. (2016), have used this technique as well. We extract the 1D radial profiles from both epochs, with uncertainties on each data point, then shift epoch 1 relative to epoch 2, minimizing the value of χ^2 . Profiles are extracted in pixel space (X-ray pixel: 0.492”, radio pixel: 0.4”), with shifts calculated on a grid of 2000 points with a size of 0.025 pixels. We only fit for the shift within an area (specific to each region) containing the filament edge, as shown in Figure 2.

While we use identical regions in both the X-ray and radio, there are slight differences in the way that we calculate the uncertainties on the profiles. For the X-ray band, we work in photon counts, and take the square root of the number of counts in each pixel as the uncertainty. The radio images are in units of Jy beam^{-1} , and we consider the “noisiness” of the image to be the main source of uncertainty. We calculate the rms dispersion within the off-source background, effectively a flat-field. We obtain uncertainties of 8.5×10^{-5} and 4.0×10^{-5} Jy beam^{-1} for the 1984 and 2013 images, respectively, and apply these constant uncertainty values to all points along their respective radio profiles. For both the X-ray and radio profiles, reduced χ^2 values were generally close to 1.

⁷<http://ds9.si.edu/site/Home.html>

For the uncertainties on the proper motion measurements themselves, we include estimates of both the statistical and systematic uncertainties. The statistical errors are the 90% confidence limits resulting from a χ^2 increase of 2.706. The 90% uncertainties in each direction are virtually identical, so we average them for a single number. For the systematic errors, the uncertainties arising from different WCS alignments are negligible. However, what is not trivial is the angle of the projection box to the shock front. Following a procedure similar to Katsuda et al. (2008b), we vary the angle of the projection box by 1 and 2° in both directions with respect to the shock front for each region and re-measure the proper motion. To be conservative, we adopt the 2° variation as the measure of our systematic uncertainty. As with the statistical uncertainties, because the values in each direction are similar, we average them together for a single value.

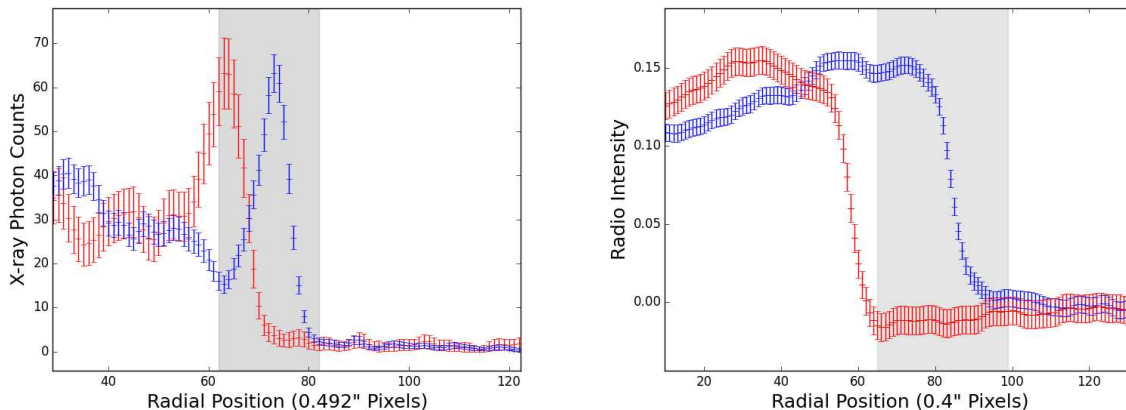


Fig. 2.— Two examples of “well-behaved” profiles. In all plots, the first epoch is shown in red and the second in blue. *Left*: An example of an X-ray profile (region 13; P.A. 255°). *Right*: An example of a radio profile (region 11, P.A. 213°). Shaded areas mark regions where the fit was performed.

The vast majority of our regions are “well-behaved,” in that the shape of the profile is virtually identical in both epochs. We show an example of a well-behaved profile in X-ray and radio in Figure 2. However, there are a few regions where this is not the case. We show the worst

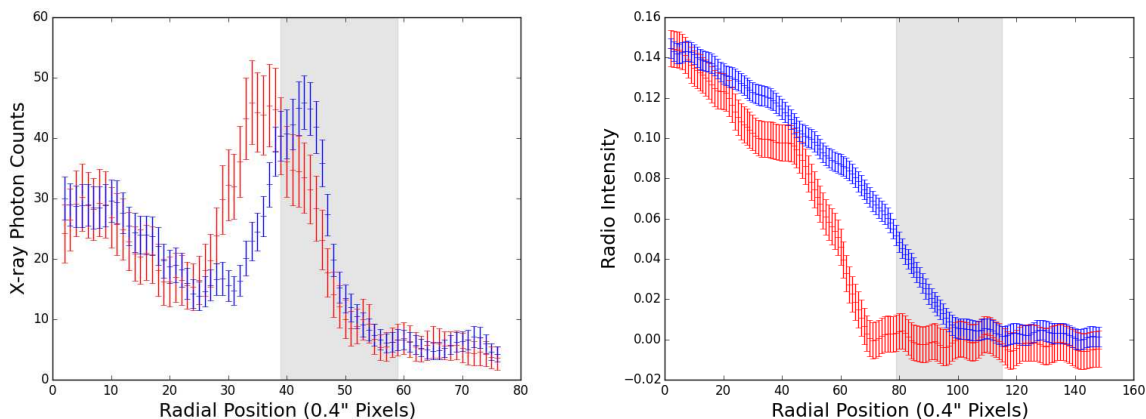


Fig. 3.— The worst-case profiles in X-ray and radio. *Left:* The X-ray profiles from region 3 (P.A. 62°). *Right:* The radio profile from region 15 (P.A. 295°).

example from each wavelength regime in Figure 3. In the X-ray band, region 3 (P.A. 62°) is shown, where the profile clearly changes shape between the 2000 and 2015 data. We do report a proper motion here, defining it as the shift in the leading edge of the shock front, when the profile rises above the level of the background. This region is even worse in the radio (not shown), where no clear shock front is present and the profile simply gently fades into the background. We do not report a radio proper motion for this region.

Region 15 (PA 295°) is shown as our “worst-case” (with the exception of region 3, discussed above) radio profile. The profile becomes more elongated between the two epochs, for reasons that are unknown. Nonetheless, we apply the same technique as above by fitting the shift of the leading edge of the shock. This leads to a value of the proper motion, as reported in Table 1, but this value should be used with caution. Interestingly, the X-ray profiles from this region do not show this behavior.

The results of our measurements are given in Table 1 and Figure 4. We confirm the existence of a clear velocity gradient in the shock speeds. Even if we disregard the potentially problematic X-ray measurement of region 3 (discussed above), we still see a difference of approximately a

factor of 2 in the expansion velocities between the E/NE portions of the remnant and the W/SW. Furthermore, with a few exceptions, the X-ray and radio proper motions agree within errors. The biggest discrepancy occurs in region 15, which we have already pointed out is problematic.

While we report all proper motions in units of arcsec yr⁻¹, a conversion to velocity relies upon the distance to Tycho, which may lie from 2.3 to 4 kpc. If we adopt a fiducial distance of 3 kpc, the conversion factor is 0.1'' yr⁻¹ ≡ 1422 km s⁻¹. This distance would imply maximum shock velocities of about 5300 km s⁻¹, consistent with the low pre-shock densities reported in W13, Katsuda et al. (2010), and Cassam-Chenaï et al. (2007). It is interesting to note that our region 4 corresponds to the well-known optical “knot-G” of Kamper & van den Bergh (1978), and the proper motion we measure is fully consistent with their value of 0.20 ± 0.01'' yr⁻¹.

4. An Off-center Explosion Site

In W13, we described hydrodynamical simulations of a spherically-symmetric SN explosion into a density gradient in the ISM, which is the simplest explanation for the different densities and shock velocities found around the remnant’s periphery. This leads to a remnant where the geometric center *cannot* be the site of the original explosion. We showed that the remnant can still be remarkably round, despite higher expansion velocities on one side.

An important result of these simulations, discussed in W13, is that the ratio of the velocity semi-amplitude $(V_{max} - V_{min})/(V_{max} + V_{min})$ to the radial offset from the center of the explosion $(R_{max} - R_{min})/(R_{max} + R_{min})$ is roughly constant at a value of 2.2 ± 0.1 for ages between about 300 and 700 year. With our refined proper motion measurements presented here, we can more accurately calculate the radial offset necessary to explain the observations.

We use the average of the X-ray and radio proper motions given in Table 1, omitting region 3, as this has an unusually low X-ray proper motion and no measureable radio value. We use a

χ^2 minimization algorithm to fit a sinusoidal function, $F = A \sin(\theta + \phi) + Y$ to the data shown in Figure 4, for both the amplitude, A , and the vertical offset, Y , in units of arcsec yr^{-1} , as well as for the phase, ϕ . In this formalism, $V_{max} = Y + A$ and $V_{min} = Y - A$, and the velocity semi-amplitude reduces to A/Y . We obtain best-fit values of $A = 0.062 \pm 0.0045$ and $Y = 0.293 \pm 0.002$, leading to a velocity semi-amplitude of 0.212 ± 0.015 . Dividing this by the ratio of 2.2 gives an offset of $(9.6 \pm 0.7)\%$ of the radius of the remnant, or $(23 \pm 1.7)''$, with the offset in the V_{min} direction, which occurs in the NE at a position angle of $51^\circ \pm 4.8^\circ$ with respect to the geometric center of Ruiz-Lapuente et al. (2004). This is comparable to the search radius of Kerzendorf et al. (2013) (who found no viable candidate for a remaining donor star under the single-degenerate Type Ia SN scenario), and that of Ruiz-Lapuente et al. (2004), who report a possible candidate. This candidate, “Star G,” is $31.4''$ from our explosion center.

This is in contrast to Xue & Schaefer (2015), who find an offset in the NW direction. This results in a large ($48.2''$) displacement between our best-fit explosion center, located at $\alpha = 0^h 25^m 22.6^s$ and $\delta = 64^\circ 8' 32.7''$, and their results. We note, though, that their paper uses the previously reported X-ray and radio proper motion measurements of R97 and K10. Also, our results are based on 2D hydrodynamical simulations instead of a thin-shell approximation that is strictly valid only for spherically-symmetric remnants. Whatever the status of the companion star in Tycho, we stress that a circular morphology does not guarantee an explosion site in the center of the remnant.

5. Conclusions

New observations of Tycho with *Chandra* in 2015 and the VLA in 2013/14 have stretched the baselines for proper motion measurements of the forward shock to 12-15 year and ~ 30 year, respectively. We applied a self-consistent approach to both data sets, refining previous proper motion measurements. The shock velocity in Tycho varies by approximately a factor of

two from one side of the remnant to the other, consistent with previous measurements, and with density variations inferred from *Spitzer* observations. This leads to an offset of about 10% of the remnant's radius between the geometric center of the remnant and the site of the explosion. Despite the circular appearance of Tycho, offsets such as this could exist in remnants of other SNe as well, impacting the search for surviving companion stars.

Support for this work was provided through Chandra Award GO4-15074Z issued by the Chandra X-ray Observatory Center, which is operated by the Smithsonian Astrophysical Observatory for and on behalf of NASA under contract NAS8-03060. NRAO is a facility of the NSF operated under cooperative agreement by Associated Universities, Inc. LC acknowledges NSF AST-1412980.

Table 1. Proper Motions as a Function of Position Angle

Reg	Deg	Width	X-ray PM	χ^2 (d.o.f.)	Stat, Syst	Radio PM	χ^2 (d.o.f.)	Stat, Syst
1	15	64	0.265	7.48 (9)	0.0104, 0.0127	0.318	13.9 (13)	4.59×10^{-3} , 9.85×10^{-3}
2	30	48	0.218	8.64 (13)	0.0224, 6.54×10^{-3}	0.317	16.5 (18)	4.52×10^{-3} , 8.25×10^{-3}
3	62	26	0.063	36.2 (18)	0.0371, 8.87×10^{-3}
4	80	40	0.193	12.9 (12)	0.0104, 0.0184	0.205	20.7 (22)	8.33×10^{-3} , 0.0145
5	101	30	0.243	21.3 (28)	0.0300, 0.0187	0.273	41.1 (38)	5.70×10^{-3} , 8.46×10^{-3}
6	118	47	0.281	14.8 (15)	0.0194, 0.0126	0.345	44.3 (38)	5.38×10^{-3} , 4.84×10^{-3}
7	143	32	0.306	17.8 (22)	0.0461, 0.0321	0.319	33.9 (36)	0.0106, 9.90×10^{-3}
8	153	20	0.319	24.3 (30)	0.0463, 0.0112	0.300	26.9 (28)	6.56×10^{-3} , 0.0138
9	173	35	0.333	15.7 (20)	0.0168, 7.33×10^{-3}	0.328	36.8 (38)	4.26×10^{-3} , 4.59×10^{-3}
10	185	30	0.337	16.1 (18)	0.0187, 3.07×10^{-3}	0.347	16.7 (20)	6.23×10^{-3} , 4.85×10^{-3}
11	213	44	0.336	18.3 (23)	0.0137, 9.74×10^{-3}	0.359	39.7 (33)	4.92×10^{-3} , 7.54×10^{-3}
12	236	47	0.334	20.2 (25)	9.84×10^{-3} , 2.47×10^{-3}	0.364	27.2 (24)	7.08×10^{-3} , 0.0120
13	255	42	0.298	20.6 (18)	8.26×10^{-3} , 5.07×10^{-3}	0.340	19.0 (22)	9.90×10^{-3} , 0.0122
14	276	20	0.337	12.2 (16)	9.77×10^{-3} , 0.0216	0.408	21.0 (18)	0.0130, 0.0306
15	295	37	0.229	17.2 (19)	0.0133, 0.0124	0.366	121.2 (38)	0.0220, 0.0275
16	312	42	0.305	28.7 (24)	7.63×10^{-3} , 4.34 ± 0.67	0.311	23.6 (20)	3.93×10^{-3} , 6.52×10^{-3}
17	333	42	0.170	16.2 (12)	0.0147, 8.48×10^{-3}	0.242	17.7 (22)	3.61×10^{-3} , 3.39×10^{-3}

Note. — Deg = Position angle, east of north, with respect to geometric center of Ruiz-Lapuente et al. (2004). Width of regions in arcseconds. Proper motions (PM) in arcseconds yr⁻¹. Stat and Syst refer to the statistical and systematic uncertainties, respectively, on the proper motions.

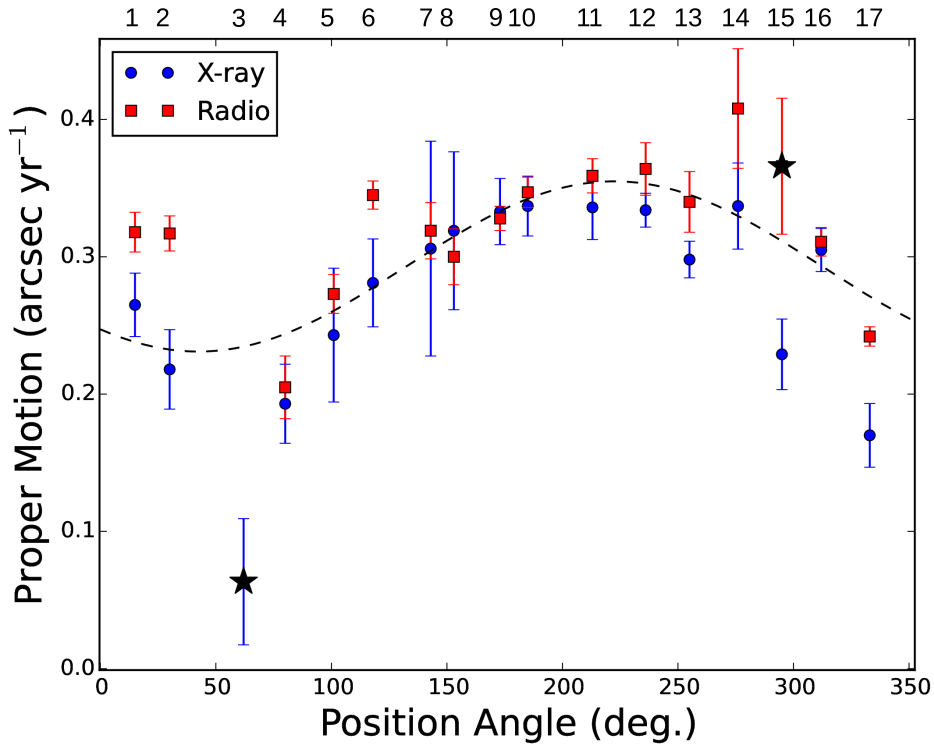


Fig. 4.— The proper motions in all of our regions for both X-rays and radio. Region number is given along the top of the plot. Error bars plotted are the linear sum of both the statistical and systematic uncertainties. The sinusoidal fit described in the text is shown as dashed line. Black stars mark the “bad” data points shown in Figure 3.

REFERENCES

- Albinson, J.S., Tuffs, R.J., Swinbank, E., & Gull, S.F. 1986, *MNRAS*, 219, 427
- Baade, W. 1945, *ApJ*, 102, 309
- Cassam-Chenaï, G., Hughes, J.P., Ballet, J., & Decourchelle, A. 2007, *ApJ*, 665, 315
- Chevalier, R.A., Kirshner, R.P., & Raymond, J.C. 1980, *ApJ*, 235, 186
- Hughes, J.P. 2000, *ApJ*, 545, 53
- Hwang, U., Decourchelle, A., Holt, S., Petre, R. 2002, *ApJ*, 581, 1101
- Katsuda, S., Tsunemi, H., & Mori, K. 2008a, *ApJ*, 678, 35
- Katsuda, S., Tsunemi, H., Uchida, H., & Kimura, M. 2008b, *ApJ*, 689, 225
- Katsuda, S., Petre, R., Hughes, J.P., Hwang, U., Yamaguchi, H., Hayato, A., Mori, K., Tsunemi, H. 2010, *ApJ*, 709, 1387
- Kamper, K.W. & van den Bergh, S. 1978, *ApJ*, 224, 851
- Kerzendorf, W.E., et al. 2013, *ApJ*, 774, 99
- Krause, O., Tanaka, M., Usuda, T., Hattori, T., Goto, M., Birkmann, S., & Nomoto, K. 2008, *Nature*, 456, 617
- Ressler, S.M., Katsuda, S., Reynolds, S.P., Long, K.S., Petre, R., Williams, B.J., & Winkler, P.F. 2014, *ApJ*, 790, 85
- Rest, A., et al. 2008, *ApJ*, 681, 81
- Reynolds, S.P. & Keohane, J.W. 1999, *ApJ*, 525, 368

Reynoso, E.M., Moffett, D.A., Goss, W.M., Dubner, G.M., Dickel, J.R., Reynolds, S.P., & Giacani, E.B. 1997, *ApJ*, 491, 816

Ruiz-Lapuente, P., et al. 2004, *Nature*, 431, 1069

Schaefer, B.E. & Pagnotta, A. 2012, *Nature*, 481, 164

Schwarz, U.J., Goss, W.M., Kalberla, P.M., & Benaglia, P. 1995, *A&A*, 299, 193

Stephenson, F.R. & Green, D.A. 2002, *Historical Supernovae and their Remnants*, Oxford University Press

Tran, A., Williams, B.J., Petre, R., Ressler, S.M., & Reynolds, S.P. 2015, *ApJ*, 812, 101

Webbink, R.F. 1984, *ApJ*, 277, 355

Whelan, J., & Iben, I., Jr. 1973, *ApJ*, 186, 1007

Williams, B.J., et al. 2013, *ApJ*, 770, 129

Winkler, P.F., et al. 2014, *ApJ*, 781, 65

Xue, Z. & Schaefer, B.E. 2015, *ApJ*, 809, 183

Yamaguchi, H., Katsuda, S., & Castro, D. et al. 2016, *ApJ*, 820, 3